

## Accepted Manuscript

Infrared thermography-based evaluation of the elastic-plastic j-integral to correlate fatigue crack growth data of a stainless steel

G. Meneghetti, M. Ricotta, G. Pitarresi

PII: S0142-1123(19)30013-1  
DOI: <https://doi.org/10.1016/j.ijfatigue.2019.03.034>  
Reference: JIJF 5049

To appear in: *International Journal of Fatigue*

Received Date: 15 January 2019  
Revised Date: 27 February 2019  
Accepted Date: 22 March 2019

Please cite this article as: Meneghetti, G., Ricotta, M., Pitarresi, G., Infrared thermography-based evaluation of the elastic-plastic j-integral to correlate fatigue crack growth data of a stainless steel, *International Journal of Fatigue* (2019), doi: <https://doi.org/10.1016/j.ijfatigue.2019.03.034>

This is a PDF file of an unedited manuscript that has been accepted for publication. As a service to our customers we are providing this early version of the manuscript. The manuscript will undergo copyediting, typesetting, and review of the resulting proof before it is published in its final form. Please note that during the production process errors may be discovered which could affect the content, and all legal disclaimers that apply to the journal pertain.



# INFRARED THERMOGRAPHY-BASED EVALUATION OF THE ELASTIC-PLASTIC J-INTEGRAL TO CORRELATE FATIGUE CRACK GROWTH DATA OF A STAINLESS STEEL

G. Meneghetti<sup>a),\*</sup>, M. Ricotta<sup>a)</sup>, G. Pitarresi<sup>b)</sup>

<sup>a)</sup> University of Padova, Department of Industrial Engineering, Via Venezia, 1, 35131 Padova – Italy

<sup>b)</sup> University of Palermo, Department of Engineering, Viale delle Scienze, 90128, Palermo - Italy

Corresponding author: Giovanni Meneghetti, [giovanni.meneghetti@unipd.it](mailto:giovanni.meneghetti@unipd.it)

## ABSTRACT

The elastic-plastic J-integral is adopted to correlate fatigue crack growth data of ductile metals. An analytical link is known to exist between the J-integral and the strain energy density averaged in a control volume embracing the crack tip. On the other hand, the strain energy fluctuation is the source of temperature variations close to a fatigue crack tip of a metal material; hence the possibility to measure the J-integral from infrared thermographic scanning at the crack tip is envisaged and it is the focus of this paper. It is proposed that the elastic component of the J-integral is derived from a thermoelastic stress analysis, while the plastic component of the J-integral is derived from the heat energy loss. An analytical expression is formalised to apply this novel approach. Therefore, the elastic-plastic J-integral range was evaluated starting from infrared temperature maps measured in situ during crack propagation tests of AISI 304L stainless steel specimens. The range of the infrared thermography-based J-integral correlated well the crack growth data generated in small as well as large scale yielding conditions. Finally, the experimental values of the J-integral were successfully compared with the corresponding numerical values obtained from elastic-plastic finite element analyses.

**KEYWORDS:** Fracture Mechanics, crack tip plasticity, crack tip thermoelastic stress analysis, energy methods, fatigue, temperature, J-integral

**NOMENCLATURE**

$a$  = notch depth plus notch-emanated crack length [m]

$c$  = material specific heat [J/(kg·K)]

$c_p$  = material specific heat at constant pressure [J/(kg·K)]

$f_{acq}$  = sampling rate of the infrared camera [Hz]

$f_L$  = load test frequency [Hz]

$h$  = specific thermal flux [W/m<sup>2</sup>]

$n'$  = cyclic strain hardening exponent

$n_{max}$  = number of acquired infrared images

$r_n$  = notch radius [mm]

$t_k$  = specimen thickness [m]

$w$  = specimen gross width [mm]

$E$  = material elastic modulus [MPa]

$\dot{E}_s$  = rate of accumulation of stored energy averaged over one loading cycle [W/m<sup>3</sup>]

$J; \Delta J, J_{max}$  = J-integral; its range, its maximum value in a fatigue cycle [J/m<sup>2</sup>]

$J_e, J_{max,e}$  = elastic component of J; its maximum value in a fatigue cycle [J/m<sup>2</sup>]

$J_p, J_{max,p}$  = plastic component of J; its maximum value in a fatigue cycle [J/m<sup>2</sup>]

$K_I, \Delta K_I$  = mode I stress intensity factor, its range [MPa·m<sup>0.5</sup>]

$K'$  = cyclic strength coefficient [MPa]

$K_{TH}$  = thermoelastic constant [MPa<sup>-1</sup>]

$R_c$  = radius of the material control volume  $V_c$  [m]

$Q$  = heat energy exchanged by a unit volume of material [J/m<sup>3</sup>]

$\bar{Q}$  = heat energy exchanged by a unit volume of material per cycle [J/(m<sup>3</sup>·cycle)]

$\dot{Q}$  = heat energy rate exchanged by a unit volume of material [W/m<sup>3</sup>]

$\bar{\dot{Q}}$  = average heat energy rate exchanged by a unit volume of material ( $\dot{Q}$  averaged over one loading cycle) [W/m<sup>3</sup>]

$\bar{Q}^*$  = heat energy per cycle averaged in the volume  $V_c$  [J/(m<sup>3</sup>·cycle)]

$T$  = material temperature [K]

$\bar{T}$  = material temperature averaged over one loading cycle [K]

$T_o$  = initial material temperature at each thermoelastic acquisition [K]

$\dot{U}$  = rate of variation of internal energy per unit volume of material [W/m<sup>3</sup>]

$V_c$  = material control volume [m<sup>3</sup>]

$W$  = plastic strain energy density [J/m<sup>3</sup>]

$\bar{W}$  = plastic strain energy density per cycle [ $\text{J}/(\text{m}^3 \cdot \text{cycle})$ ]

$\dot{W}$  = plastic strain energy rate [ $\text{W}/\text{m}^3$ ]

$\bar{\dot{W}}$  = average plastic strain energy rate ( $\dot{W}$  averaged over one loading cycle) [ $\text{W}/\text{m}^3$ ]

$W_{CC}$  = elasto-plastic strain energy density (strain energy density evaluated under the cyclic stress-strain curve) [ $\text{J}/\text{m}^3$ ]

$W_{CC,e}$  = elastic component of  $W_{CC}$  [ $\text{J}/\text{m}^3$ ]

$W_{CC,p}$  = plastic component of  $W_{CC}$  [ $\text{J}/\text{m}^3$ ]

$\tilde{W}_{CC}$  = elasto-plastic strain energy included in the structural volume [J]

$\tilde{W}_{CC,e}$  = elastic component of  $\tilde{W}_{CC}$  [J]

$\tilde{W}_{CC,p}$  = plastic component of  $\tilde{W}_{CC}$  [J]

$\alpha$  = isotropic coefficient of thermal expansion [ $\text{K}^{-1}$ ]

$\lambda$  = material thermal conductivity [ $\text{W}/(\text{m} \cdot \text{K})$ ]

$\nu$  = material Poisson's coefficient

$\rho$  = material density [ $\text{kg}/\text{m}^3$ ]

$\sigma_g$  = applied gross-section stress [MPa]

$\sigma_{ii}$  = linear stress invariant (sum of normal stresses) [MPa]

$\sigma_n$  = applied net-section stress [MPa]

$\sigma_{p02}$  = engineering proof stress [MPa]

$\sigma'_{p02}$  = cyclic proof stress [MPa]

## 1. INTRODUCTION

Fatigue of metallic materials is a dissipative phenomenon involving plastic deformations that require a certain amount of work done on the material. A certain part of this energy is dissipated as heat [1], which induces some temperature increase of the material during fatigue testing. Concerning Fracture Mechanics problems, in the last decades several temperature-related studies were carried-out, as the local heating at the crack tip [2-4], the crack propagation assessment based on the hysteresis energy [5-16], the thermal effects on stress intensity factors [17,18], the plastic

zone size evaluation and the heat energy dissipation at the crack tip [19-27] and the correlation of energy dissipation at the crack tip with the J-integral [28-30].

Recently, a relation between Rice's J-integral [31] and the heat energy per cycle averaged in a control volume embracing the crack tip (the  $\bar{Q}^*$  parameter) has been put forward [29], under the simplifying assumption that the elastic strain energy close to the crack tip is negligibly small if compared to the plastic strain energy. The heat energy involved in such relation was evaluated experimentally starting from the temperature field measured close to the fatigue crack tip by means of an infrared camera; then, by virtue of being related to the J-integral, it was adopted as an elastic-plastic Fracture Mechanics driving force to correlate crack growth data generated from tension-compression axial fatigue tests of specimens machined from 4-mm-thick, hot-rolled AISI 304L steel plates [29]. While the reader is referred to [29] for additional details, here we recall that the control volume  $V_c$ , where the heat energy was averaged, has been determined by equalling the averaged heat energy in cracked and plain specimens for the same fatigue life; as a result,  $R_c=0.52$  mm was obtained.

The aforementioned simplifying hypothesis that the elastic strain energy close to the crack tip is negligibly small if compared to the plastic strain energy implies a limitation of applicability of the approach outlined previously [29]. Such a limitation is removed in the present paper, because the elastic component of the J-integral has been included in the experimental evaluation of the total J-integral. Practically, the same thermograms acquired to evaluate  $\bar{Q}^*$  have been exploited to estimate the mode I Stress Intensity Factor  $K_I$  by means of the Thermoelastic Stress Analysis (TSA) and eventually to obtain the elastic J-integral. The advantage of such experimental evaluation is that the measured SIF inherently considers the real stress field acting on the specimen, regardless of the knowledge of exact loading or boundary conditions.

It is renowned that TSA is able to retrieve a full field map of the first stress invariant, after filtering out the thermoelastic signal from the acquired thermograms [32]. Classical formulations of the stress field as a function of the SIF, taken from Linear Elastic Fracture Mechanics, can be fitted

with the experimental thermoelastic signal; as a result an estimation of  $\Delta K_I$  is obtained,  $\Delta K_I$  being the peak-to-peak SIF range under a cyclic loading [33]. A number of analytical formulations and fitting algorithms have been proposed for this purpose [33-37]. Some more recent works have also used the experimental  $\Delta K_I$ , obtained from TSA, to characterise the full Paris law by a purely elastic approach [38-40]. Some authors have tried to exploit the information from the thermoelastic maps to retrieve and monitor the crack tip position during a fatigue test [40]. Furthermore, the Thermoelastic signal phase and Second Harmonic maps have also been looked over as potential indicators of the plastic zone size and of local loss of adiabaticity [26][39]; some authors explored also the influence of motion compensation on the analyses [41]. Following on this state of the art, the present work has implemented the method from Stanley and Chan [34] to evaluate the SIF from TSA, by measuring both the First and Second Harmonic signals with a Discrete Fourier Transform approach [42], and pre-treating all acquired thermograms with motion-compensation.

In summary, the non-contact, infrared thermography-based analyses of energy dissipation and thermoelastic response at the crack tip led to the evaluation of the plastic and elastic component of the J-integral, respectively. Eventually, the elastic-plastic J-integral was adopted to correlate crack growth data of stainless steel specimens generated in small scale as well as large scale yielding conditions.

## **2. THEORETICAL BACKGROUND**

### **2.1 Heat dissipation at the crack tip**

A quantitative evaluation of energy exchanges involved in fatigue has been performed several decades ago [43]. From a thermomechanical point of view, fatigue can be considered a dissipative and quasi-static process according to the classical continuum mechanics reported in ref. [44][45]. It is well known that the energy balance equation can be written in terms of power per unit volume by introducing the Helmholtz free energy as a thermodynamic potential [45-48]. If the power quantities

appearing in the energy balance equation are averaged over one fatigue loading cycle, then it can be written [29]:

$$\rho c \dot{\bar{T}} - \lambda \nabla^2 \bar{T} = \dot{\bar{W}} - \dot{\bar{E}}_s \quad (1)$$

where  $\bar{W}$  is the plastic strain energy per cycle and  $\bar{E}_s$  is the stored energy per cycle. To derive Eq. (1) starting from the general energy balance equation, the following observations deserve to be mentioned [29]:

- the contribution of the thermoelastic heat source in Eq.(1) vanishes because it consists in a reversible exchange between mechanical and thermal energy, which does not produce a net energy dissipation or absorption over one loading cycle [1,49-51];
- the dependence of the material state on temperature is neglected, because temperature variations are small if compared to that necessary for phase transformation generating the coupling heat source in the form of latent heat

By introducing the internal energy rate  $\dot{U}$  according to the definition given by Rousselier [47]:

$$\dot{U} = \rho \cdot c \cdot \dot{\bar{T}} + \dot{\bar{E}}_s \quad (2)$$

and letting:

$$\dot{\bar{Q}} = \lambda \nabla^2 \bar{T} \quad (3)$$

then Eq. (1) becomes:

$$\dot{U} = \dot{\bar{W}} + \dot{\bar{Q}} \quad (4)$$

The energy balance Eq. (4) is illustrated in Figure 1a, which shows **Error! Reference source not found.**the positive energy exchanges involved, i.e. the mechanical energy rate  $\dot{\bar{W}}$  and the heat energy rate  $\dot{\bar{Q}}$ .

Since all energy contribution have been averaged over one loading cycle, Eq. (1) describes the evolution of the average temperature per cycle  $\bar{T}(x,y,z;t)$ , which is depicted in Figure 1b qualitatively. On the contrary, thermoelastic oscillations that are indeed superimposed to the average temperature signal are quantitatively shown in next Figure 3, which will be commented later on.

The specific heat loss  $\bar{Q}$  can now be averaged in a volume  $V_c$  surrounding the tip of the crack (see Figure 2), according to the following expression [27]:

$$\bar{Q}^* = \frac{1}{V_c} \int_{V_c} \bar{Q} \cdot dV \Rightarrow -\frac{1}{f_L V_c} \cdot \int_{S_{cd}} \bar{h} \cdot dS \quad (5)$$

where the heat flux  $\bar{h}$  is integrated in the portion of the boundary of  $V_c$ ,  $S_{cd}$ , through which heat energy is transferred by conduction. The hypothesis that the heat is extracted from  $V_c$  only by conduction is not true, strictly speaking. However, it has been demonstrated that conduction is by far the most active heat transfer mechanism in standard laboratory testing conditions [27]. It is worth noting also that while the observed temperature field depends on the applied load test frequency,  $f_L$ , the thermal energy transferred from the crack tip to the surroundings,  $\bar{Q}^*$ , does not [52]. The heat flux  $\bar{h}$  can be evaluated from the thermal gradients calculated from infrared temperature maps; therefore, referring to a two-dimensional problem, Eq. (5) can be written as follows [27]:



$$\bar{Q}^* = \frac{1}{f_L V_c} \cdot \lambda \cdot t_k \cdot R_c \cdot \int_{-\pi}^{+\pi} \frac{\partial \bar{T}(r, \theta)}{\partial r} \Big|_{r=R_c} \cdot d\theta \quad (6)$$

$\bar{T}(r, \theta)$  being the average temperature per cycle measured after the thermal equilibrium with surroundings is achieved, as shown in Figure 3, which reports a typical temperature vs time acquisition at a point inside  $V_c$  after a fatigue test has started. If the temperature field is monitored by means of an infrared camera, Figure 3a is the pixel-by-pixel temperature vs time history and it shows that temperature increases until the mean level stabilizes and the alternating component due to the thermoelastic effect is superimposed (see Figure 3b). To calculate the average temperature field  $\bar{T}(r, \theta)$  in Eq. (6) let us consider a sampling window taken after thermal equilibrium with the surroundings is achieved (between  $t_s$  and  $t^*$  in Figure 3a); the average temperature  $T_m^i$  referred to the  $i$ -th pixel is defined as follows:

$$T_m^i = \frac{\sum_{j=1}^{n_{\max}} T_j^i}{n_{\max}} \quad (7)$$

where  $T_j^i$  are the temperature data acquired at a sampling rate  $f_{\text{acq}}$  and  $n_{\max} = f_{\text{acq}} \cdot (t^* - t_s)$  is the number of picked-up samples between the start time  $t_s$  ( $j=1$ ) and the end time  $t^*$  ( $j=n_{\max}$ ).

## 2.2. J-integral estimations from the temperature field

In the open literature (see ref [53-55], as examples), the Rice's J-integral [31] is adopted as driving force to rationalise crack growth data in small as well as large scale yielding conditions. J can be evaluated by adding its elastic,  $J_e$ , and plastic,  $J_p$ , contributions (see [54,55], as examples):

$$J = J_e + J_p \quad (8)$$

Evaluating the elastic contribution,  $J_e$ , is very straightforward since it can be calculated according to Eq.9a and 9b, for plane stress or plane strain conditions, respectively:

$$J_{\max,e} = \frac{K_{I,\max}^2}{E} \quad (9a)$$

$$J_{\max,e} = \frac{K_{I,\max}^2 \cdot (1 - \nu^2)}{E} \quad (9b)$$

$K_I$  being the linear elastic stress intensity factor for the same applied external load [54,55]. The experimental evaluation of the elastic and plastic components of the J-integral starting from infrared thermograms is reported in detail in the next sections.

### 2.2.1 Evaluating Mode I Stress Intensity factor by the Thermoelastic Stress Analysis

Under linear elastic straining conditions, the material undergoes a local volume change that is associated to a reversible temperature change. This correlation is known as the Thermoelastic Effect, and a well-established theoretical framework, originating from the work of Lord Kelvin, has led to the following analytical representation[32,56]:

$$\Delta T = -T_o \frac{\alpha}{\rho c_p} \Delta \sigma_{ii} = -T_o K_{TH} \Delta \sigma_{ii} \quad (10)$$

The above equation requires that the material is isotropic and undergoing adiabatic transformation, which is practically achieved by applying a cyclic loading above a suitable threshold frequency. Applying a cyclic sinusoidal loading brings in another useful practicality, i.e. the temperature change due to the thermoelastic effect ( $\Delta T$  in Eq. 10) is modulated at the same frequency of the applied load. This phenomenon led to a technique, generally referred to as Thermoelastic Stress Analysis (TSA), that evaluates the thermoelastic temperature change  $\Delta T$  by applying narrow band-pass harmonic filtering on the acquired temperature fluctuation [42].

Therefore, TSA is able to provide a map of the linear stress invariant (i.e. of isopachics) associated to a crack length and hence enables one to derive the  $\Delta K_I$  value, i.e. the peak-to-peak variation of the elastic stress intensity factor.

A number of methods have been developed to obtain  $\Delta K_I$  from maps of  $\Delta\sigma_{ii}$  measured around the crack tip [33]. These basically consist in fitting the experimental values of  $\Delta\sigma_{ii}(x,y)$  to analytical models of the stress field, derived from Linear Elastic Fracture Mechanics. The method applied in this work was originally proposed by Stanley and Chan [34] and is briefly summarised here. In the case that the IR equipment is able to provide calibrated maps of the temperature, then the thermoelastic signal range can be written from Eq.(10) as:

$$\Delta\sigma_{ii} = -\frac{1}{-T_0 K_{TH}} \Delta T \quad (11)$$

By using the Westergard's equations representing the stress field, over the area dominated by  $K_I$ , Eq.(11) can be written also as:

$$\Delta(\sigma_{xx} + \sigma_{yy}) = \frac{2\Delta K_I}{\sqrt{2\pi r}} \left[ \cos\left(\frac{\theta}{2}\right) + \sin\left(\frac{\theta}{2}\right) \right] \quad (12)$$

It was found that, in pure Mode I, the maximum value of  $\Delta\sigma_{ii}$  along a line parallel to the crack line and distant  $y$  from it, is linearly correlated to  $y$  through the following relationship [34]:

$$y = \left( \frac{3\sqrt{3}}{4\pi} T_o^2 K_{TH}^2 \Delta K_I^2 \right) \frac{1}{(\Delta T_{max})^2} \quad (13)$$

By analysing the plot of  $y$  versus the experimental values of  $(1/\Delta T_{max})^2$ , a linear region is identified whose slope is a known function of  $\Delta K_I$ , once  $T_o$  and  $K_{TH}$  are known. The linear behaviour is confined to the area where the Westergard's equations, arrested to the first singular term  $K_I$ , rule. A significant advantage of the Stanley and Chan's method is that an accurate identification of the crack tip in the thermograms is not required. In fact, as shown by Eq. (13) the SIF is obtained from the angular coefficient of a linear regression involving the relative distance from the crack line,  $y$ , as the only geometric variable. Having  $K_I$  from Eq. (13), i.e. from thermographic data acquired at various time intervals during a fatigue test,  $J_e$  can be obtained from Eqs. (9).

### 2.2.2 Evaluating the plastic component of $J$ -integral

An analytical link between the  $J$ -integral of a sharp V-notch and the strain energy  $\tilde{W}_{CC}$  included in a circular volume having radius  $R_c$  and centered at the sharp V-notch tip was defined by Berto and Lazzarin [57], assuming a linear elastic material behaviour:

$$\frac{W_{CC}}{t_k} = k(2\alpha, \nu) \cdot R_c \cdot J_{max} \quad (14)$$

$k(2\alpha, \nu)$  being a parameter depending on notch opening angle ( $2\alpha$ , see Figure 2) and Poisson's ratio.

In the crack case ( $2\alpha=0$ ) and with reference to plane strain conditions, Eq. (14) can be written as follows:

$$\frac{W_{CC}}{t_k} = \frac{\frac{5}{8} - \nu}{1 - \nu} \cdot R_c \cdot J_{\max} \quad (15a)$$

Conversely, in plane stress conditions, we have:

$$\frac{W_{CC}}{t_k} = \frac{5 - 3\nu}{8} \cdot R_c \cdot J_{\max} \quad (15b)$$

It is worth noting that the analytical expression of  $k(2\alpha, \nu)$  proposed in [57] is valid only if the linear elastic strain energy included in the volume  $V_c$  can be expressed solely in terms of the mode I-linear elastic notch- stress intensity factor,  $K_I^Y$ , i.e. if the higher order terms in the stress field series expansion are negligible inside  $V_c$ .

A linear relation between  $\tilde{W}_{CC}$  and J-integral was also demonstrated in the case of an elastic-plastic material obeying a power hardening law applied to sharp V-notches, having  $2\alpha=135^\circ$ , notch tip radii equal to zero and subject to plain strain conditions [57]. The relation is valid in small as well as in large scale yielding conditions and the  $k$  parameter in Eq. (14) remains practically equal to that calculated for a linear elastic material. Lazzarin and Zappalorto [58] evaluated the plastic notch stress intensity factors for pointed V-notches under antiplane shear loading and showed that in the crack case a linear relation still exists between the mode III plastic J-integral and the plastic strain energy density included in  $V_c$ , providing  $R_c$  is sufficient small to guarantee that the plastic strain energy density can be expressed solely in terms of mode III plastic notch- stress intensity factor,  $K_{3,p}$ . However, the slope of the linear trend strongly depends on the material hardening exponent. A

linear correlation was also shown previously in the case of a cracked elastic plastic body under plane stress condition [29].

The total energy included in  $V_c$  can be separated in its elastic,  $\tilde{W}_{CC,e}$ , and plastic,  $\tilde{W}_{CC,p}$ , components, as reported in Figure 4:

$$\tilde{W}_{CC} = \int_{V_c} W_{CC} \cdot dV = \tilde{W}_{CC,e} + \tilde{W}_{CC,p} \quad (16)$$

where

$$W_{CC,e} = \int_{V_c} W_{CC,e} \cdot dV \quad (17a)$$

$$W_{CC,p} = \int_{V_c} W_{CC,p} \cdot dV \quad (17b)$$

In this paper, a linear link was established between the plastic component of the strain energy density,  $\tilde{W}_{CC,p}$ , and the plastic component of the J-integral,  $J_{max,p}$ , as it will be shown later on:

$$\frac{W_{CC,p}}{t_k} = k_p (2\alpha, n') \cdot J_{max,p} \cdot R_c \quad (18)$$

where  $k_p(2\alpha, n')$  is a constant depending on the notch opening angle and the cyclic hardening exponent.

Let us assume the generalised Ramberg-Osgood law, according to which the strain is equal to the sum of its elastic  $\varepsilon_{ij,e}$  and its plastic component  $\varepsilon_{ij,p}$ , as follows [59]:

$$\varepsilon_{ij} = \varepsilon_{ij,e} + \varepsilon_{ij,p} = \left( \frac{1+\nu}{E} s_{ij} + \frac{1-2\nu}{E} \sigma_h \delta_{ij} \right) + \left( \frac{3}{2} \frac{\sigma_e^{n'-1}}{(K')^{1/n'}} s_{ij} \right) \quad (19)$$

where the summation convention is used for repeated indices. In Eq. (19)  $\sigma_e$  is the Von Mises stress,  $s_{ij}$  is the deviatoric component of the Cauchy stress tensor,  $\sigma_h$  is the hydrostatic stress and  $\delta_{ij}$  is the Kronecker delta.

The plastic component of the strain energy density can be evaluated from the plastic strain component of Eq. (19):

$$W_{CC,p} = \frac{1}{1+n'} \cdot \frac{\sigma_e^{n'+1}}{(K')^{1/n'}} \quad (20)$$

For a Masing material [60], the plastic strain energy density per cycle,  $\bar{W}$ , can be evaluated from the Ramberg-Osgood relation according to Halford [43]:

$$\bar{W} = \frac{1-n'}{1+n'} \cdot 2\sigma_e \cdot 2 \left( \frac{\sigma_e}{K'} \right)^{\frac{1}{n'}} \quad (21)$$

Comparing Eq. (21) and Eq. (20), a link between  $\bar{W}$  and  $W_{CC,p}$  is obtained, as depicted in Figure 5:

$$\bar{W} = 4(1-n') \cdot W_{CC,p} \quad (22)$$

Substituting Eq. (22), Eq. (17b) becomes:

$$W_{CC,p} = \frac{1}{4(1-n')} \int_{V_c} \bar{W} dV \quad (23)$$

There is now a body of experimental evidence that most part of the plastic strain energy per cycle  $\bar{W}$  is converted into heat energy  $\bar{Q}$  [61-64]. Letting  $\bar{W} = \bar{Q}$  and using the definition of  $\bar{Q}^*$  (Eq. (5)), Eq. (23) can be written as follows:

$$W_{CC,p} = \frac{1}{4(1-n')} \cdot \bar{Q}^* \cdot V_c \quad (24)$$

Finally, Eq. (18) can be re-formulated to link the averaged heat energy and the plastic component of the J-integral:

$$\bar{Q}^* = \frac{4(1-n') \cdot k_p(2\alpha, n')}{\pi \cdot R_c} \cdot J_{\max,p} \quad (25)$$

Therefore, in the case of plane stress conditions, Eq.(8) can be written in terms of maximum value of the J-integral as:

$$J_{\max} = \frac{K_{I,\max}^2}{E} + \frac{\pi \cdot R_c}{4(1-n') \cdot k_p(2\alpha, n')} \cdot \bar{Q}^* \quad (26)$$

### 3. MATERIAL, SPECIMEN GEOMETRY AND TEST METHODS

Constant amplitude, fully-reversed ( $R=-1$ ), load controlled crack propagation fatigue tests were carried out on specimens prepared from 4-mm-thick, hot-rolled AISI 304L stainless steel sheets, having the mechanical properties (engineering proof stress,  $\sigma_{p0.2}$ , engineering tensile strength,  $\sigma_R$ , elongation after fracture A%, constant amplitude fatigue limit,  $\sigma_{A,-1}$ , Brinell hardness HB) and the



chemical composition listed in Table 1 [29]. All tested specimens were characterised by a 8-mm-deep crack starter, but different notch opening angle and notch tip radius. In more detail, some specimens had  $r_n=0.1$  and  $2\alpha=45^\circ$ , others  $r_n =0.15$  mm and  $2\alpha=90^\circ$ , as shown in Figure 6. The fatigue tests were carried out by using a Schenck Hydropuls PSA 100 servo-hydraulic machine, equipped with a Trio Sistemi RT3 digital controller and a 100 kN load cell. Load test frequencies  $f_L$  were set between 4 and 42 Hz, depending on the applied stress level.

After polishing both specimens surfaces and mat black painting one of the specimen's surface in order to increase the emissivity, the evolution of material temperature during the fatigue tests was monitored by using a FLIR SC7000 infrared camera (50-mm focal lens, spectral response range from 1.5 to 5.1  $\mu\text{m}$ , noise equivalent temperature difference  $< 25$  mK, frame rate  $f_{\text{acq}}$  equal to 200 Hz), equipped with an analog input interface, which was used to synchronize the force signal coming from the load cell with the temperature signal measured by the infrared camera. In order to improve the spatial resolution, a 30-mm-spacer ring was adopted, to achieve 23  $\mu\text{m}/\text{pixel}$ . On the other hand, the Field of View (FoV) was reduced to 320x256 pixels and the temperature field was acquired by positioning the crack tip itself in the centre of the FoV to avoid vignetting. During the fatigue test, thermal images were recorded at given crack lengths with a frame rate  $f_{\text{acq}}=200$  Hz for a time window equal to 5 s ( $t^*-t_s = 5$  s in figure 3a), translating into  $200 \times 5 = 1000$  acquired images. Subsequently, the temperature maps were processed by using the MotionByInterpolation tool to allow for the relative motion compensation between the fixed camera lens and the moving specimen due the sinusoidal applied load; the infrared images were then analysed to perform the Thermoelastic Stress Analysis as well as to derive  $\bar{Q}^*$ .

The procedure employed for the TSA consisted in the following steps [42]: the sequence of thermograms from each 5 sec acquisition was imported into Matlab; some points at various locations were selected and the temperature-time signal analyzed in the frequency domain by applying the Discrete Fourier Transform; the frequency carrying the thermoelastic signal,  $f_L$ , was detected on the power spectrums from the selected points; the amplitude and phase of the harmonics

at the frequencies  $f_L$  and  $2f_L$  were retrieved from each point, consisting of the Thermoelastic Signal ( $\Delta T$ ) amplitude and phase on one side and of the Second Harmonic signal (SH) amplitude and phase on the other side, respectively. The maps of the SH signal are equivalent to the D-Mode maps obtained from the FLIR commercial softwares ALTAIR LI or THESA [20,65]. The Thermoelastic constant  $K_{TH}$ , needed in Eq. (13), had been evaluated experimentally for the material investigated, resulting  $K_{TH}=3.75 \cdot 10^{-6} \text{ MPa}^{-1}$  [66].

Regarding the estimation of  $\bar{Q}^*$ , the spatial distribution of the pixel by-pixel average temperature  $T_m^i$  was calculated by averaging the available 1000 frames according to Eq. (7) using the ALTAIR 5.90.002 commercial software; finally, the  $\bar{Q}^*$  parameter was evaluated by applying Eq. (6).

After every acquisition of the aforementioned 1000 temperature frames, the fatigue test was stopped to allow the crack length to be measured by using a AM4115ZT Dino-lite digital microscope operating with a magnification ranging from 20x to 220x. The microscope and the infrared camera monitored the opposite surfaces of the specimens, as reported in Figure 7. The microscope images were used to single-out the crack tip position, which was subsequently reported in the infrared thermal images.

#### 4. CRACK GROWTH DATA AND THERMOELASTIC STRESS ANALYSIS

Figure 8 shows the Paris curve of AISI 304L stainless steel, along with the 10%-90% scatter band calculated under the hypothesis of log-normal distribution of  $da/dN$  [29]. The SIF range was evaluated by carrying out 2D linear elastic finite element analyses reported elsewhere [29]. Experimental data on the left side of the two dashed vertical lines reported in Figure 8 satisfy the conditions of applicability of the LEFM according to Eq.(27) [54], while on the right hand side of the band they do not:

$$a, (w-a), L \geq \frac{4}{\pi} \cdot \left( \frac{\Delta K_I}{2 \cdot \sigma_{p02}} \right)^2 \quad (27)$$

In Eq. (27),  $a$  is the crack length,  $w$  the specimen width ( $w=46$  mm),  $2L$  the specimen height ( $2L=90$  mm) reported in Figure 6a. The data that do not satisfy the condition of applicability of the LEFM were not included in the statistical analysis reported in Figure 8, due to the crack acceleration induced by the excessive plasticity around the crack tip, as suggested in [53]. The same data were reanalysed in terms of  $\bar{Q}^*$  evaluated for  $R_c=0.52$  mm [29] and the results are shown in Figure 9, which reports the mean curve, the 10%-90% survival probability scatter bands and the scatter index  $T_{da/dN}$ . It is seen that the crack growth rates can be rationalized with a higher level of accuracy by using the averaged heat energy  $\bar{Q}^*$ , rather than the range of the linear elastic mode I SIF  $\Delta K_I$ .

Figures 10 and 11 show some representative maps of both the amplitude and phase of the Thermoelastic and the Second Harmonic signals, obtained after the lock-in procedure outlined in Section 3. The sample selected has  $r_n=0.1$  and  $2\alpha=45^\circ$ , and the total crack length is  $a=10.05$  mm in Fig. 10 and 29.3 mm in Fig. 11, while the applied gross-section stress amplitude is 81 MPa. A cross sign in the maps indicates the crack tip position as estimated by the optical microscope. It is likely that, after the motion compensation algorithm, this position could have changed slightly. The locations used to evaluate the peak-to-peak SIF range  $\Delta K_I$  are also indicated in Figures 10 and 11. The same points are highlighted in Figure 12, where the plots of  $y$  versus  $(1/\Delta T_{\max})^2$  are shown according to Eq.(13). It is noticed that some features from the maps of Fig. 10, 11 are similar to those reported in [41], where a  $R=-1$  fatigue cycle had been also applied on a Single Edge Notched Tension steel sample. It is particularly worth noting that a significant rise of the SH amplitude is observed along the flanks of the crack and also in front of the crack tip. The flanks of the crack are

loaded in compression for half-loading cycle and are unloaded in the remaining half. Such loading modulation is probably the main responsible for the rise of a second harmonic component, the same hypothesis being reported in the literature [41]. The zone ahead of the crack tip shows a local shift of the Thermoelastic phase and a local peak of the SH amplitude. Both these perturbations are widely reported in the literature and are considered as typical occurrences at crack tips. The most consolidated explanations provided are: local loss of adiabaticity due to the steep stress gradients (which introduce a phase shift different than  $180^\circ$ ); dissipation effects introduced by the plastic work, that happens to be modulated at twice the loading frequency [65]; the dependence of material properties, such as  $E$ ,  $\nu$  and  $\alpha$ , with temperature. This last influence is renowned to lead to a Second Order formulation of the thermoelastic theory [32,56]. Such second order terms (i.e. the derivatives of material properties with temperature), are generally small and negligible, but in the case of a crack, they happen to be multiplied to the term  $1/r$ , which is singular at the crack tip, thus raising the overall effect [20].

One useful outcome from TSA is the possibility to interpret the thermoelastic signal phasegram as an indicator for non-adiabatic behaviour. In practice, zones of the phasegram where the signal is shifted by angles different from  $0^\circ$  or  $180^\circ$  with respect to the loading signal could be affected by a lack of adiabaticity. In the present work, phasegrams reported in Fig. 10b and 11b show how such phase shifting is present and confined only in the proximity of the crack tip. This is typical of singular stress fields, and is likely induced by a combination of effects: presence of high stress gradients and deviation from linear elastic behaviour. However, it is pointed out that the points that behave linearly in Fig. 12 and that have been used to evaluate  $\Delta K_I$ , are placed outside of the zones where the thermoelastic phase is significantly shifted (see Figs. 10b, 11b) and the SH amplitude is significantly high (see Figs. 10c, 11c). In light of the above, it can be concluded that the applied loading frequency of 20 Hz is sufficient for the onset of adiabatic behaviour in zones where the thermoelastic signal is quantitatively measured and used for evaluating the elastic J-integral.

It is also pointed out that no smoothing algorithms have been applied in this work. Even if a certain significant noise is observed in the thermoelastic signal in Fig. 12, the linearity of the points in  $\Delta K_I$  evaluation is satisfying and the thermoelastic values of  $\Delta K_I$  have been found to differ from the numerical values obtained from linear elastic FE analyses by generally less than 10 %. This level of approximation is comparable to that generally reported in the literature [33].

## 5. CRACK GROWTH RATES VERSUS THE EXPERIMENTAL ELASTIC-PLASTIC J-INTEGRAL

Two dimensional, plane stress, linear elastic as well as elastic-plastic finite element analyses of the tested specimens (see Figure 6) were performed in Ansys<sup>®</sup> 16.2 commercial software, by using 4-node PLANE 182 element. The cyclic curve plotted in Figure 13 was implemented, along with the Von Mises plasticity rule and the isotropic hardening behaviour. J-integral calculation was based on the domain integral approach [67] implemented in Ansys<sup>®</sup>. For more details of FE analyses, the reader is referred to [29]. Having  $J_{\max}$  and  $K_{I,\max}$  from elastic-plastic and purely elastic analyses, respectively,  $J_{\max,p}$  was calculated from Eq.(8). Figure 14 shows  $W_{cc,p}$  evaluated in a control volume  $R_c=0.52$  mm versus  $J_{\max,p}$  and it can be seen that a linear relationship can be proposed with  $k_p(2\alpha, n') = 0.869$  in Eq. (18) and a coefficient of correlation  $R^2=0.9976$ . The elastic,  $J_{\max,e}$ , and the plastic,  $J_{\max,p}$ , components relevant to the experimental tests are plotted in Figure 15, where it is seen that the  $J_{\max,p}/J_{\max,e}$  ratio spans over a range between 0.1 and 3.5 and between 3.5 and 5.5, in the case of Small Scale Yielding (SSY,  $\sigma_n \leq \sigma'_{p02}=274$  MPa) and Large Scale Yielding (LSY,  $\sigma_n > \sigma'_{p02}=274$  MPa), respectively.

Having  $k_p(2\alpha, n') = 0.869$ , Figure 16a and 16b show  $J_{\max,p}$  evaluated experimentally according to Eq. (25) versus  $R_c$  for two specimens tested with a stress amplitude  $\sigma_g=81$  MPa and  $\sigma_g=120$  MPa,

respectively. It is seen that for  $R_c$  equal to or greater than 0.4 mm,  $J_{\max,p}$  evaluated experimentally can be considered fairly constant. On the contrary, for  $R_c$  lower than 0.4 mm,  $J_{\max,p}$  depends more evidently on the control volume. In the authors' opinion, the limitation due to the geometrical resolution of the adopted infrared camera (i.e 23  $\mu\text{m}/\text{pixel}$ ) affects the results for small values of  $R_c$ . By using  $k_p(2\alpha, n') = 0.869$  and the thermoelastic values of  $K_I$ , the crack propagation data were reanalysed in terms of J-integral evaluated by means of Eq. (26). Since the fatigue tests were carried out with a load ratio  $R=-1$ , then  $\Delta J$  was assumed equal  $J_{\max}$  ( $\Delta J= J_{\max} -0$ ). The results are reported in Figure 17, along with the mean curve, the 10%-90% survival probability scatter bands and the scatter index  $T_{da/dN}$ . In the same figure, the dashed line represents the mean curve of the  $\Delta J_p$  values calculated according to Eq.(25); the dashed line is closer and closer to the solid line, the higher the applied  $\Delta J$ , i.e. the lower the elastic contribution to the total  $\Delta J$ . Since the adopted load ratio was equal to -1, a certain amount of crack closure existed during the experimental tests and it is included in the  $da/dN$  vs  $\Delta J$  curve of Figure 17. Therefore, such curve cannot be extended to load ratios different from  $R=-1$  adopted here. Even though crack closure effects have not been analysed in the present work, it is worth mentioning some experimental investigations, where  $\Delta K_I$  values measured by means of the TSA have been compared with theoretical values for different applied load ratios [68,69]. As a result, it was noted that the TSA data matched the theoretical values at progressively higher applied R ratios. Conversely, at relatively low R ratios, thermoelastic SIFs were lower than the theoretical ones. The Authors pointed out that crack closure was the reason for this phenomenon.

Finally, Figure 18 shows that the FE values of the  $\Delta J$  are in very good agreement with the 10-90% survival probability scatter- band fitted on infrared thermography-based measurements of  $\Delta J$  according to Eq.(26), which is reported in previous Figure 17.

## CONCLUSIONS

In this paper, an experimental procedure to evaluate the J-integral during a fatigue test is presented and discussed. Such a procedure is based on the measurement of the temperature map around the tip of the fatigue crack, by using an infrared camera having high temperature accuracy and spatial resolution. The proposed methodology evaluates separately the elastic and plastic contributions to the total J-integral. The elastic component is calculated from the experimental evaluation of the mode I Stress Intensity Factor by means of the Thermoelastic Stress Analysis. The plastic component of J is estimated from the specific heat loss per cycle averaged over a control volume of material; the underlying engineering assumption is that the plastic strain hysteresis energy per cycle is fully converted into heat, which is supported by a body of experimental evidence reported in the literature. This approach is summarized by the Eq. (26). The proposed approach is restricted to 2D problems and has the same limitations of applicability of the Thermoelastic Stress Analysis, particularly concerning the adiabaticity requirements at the locations where the elastic component of the J-integral is evaluated.

The infrared thermography-based method to evaluate the elastic-plastic J-integral has been applied to fatigue crack growth data generated from push-pull, axial fatigue tests of 4-mm-thick hot rolled AISI 304L stainless steel specimens. The crack propagation data were correlated in terms of range of the elastic-plastic J-integral, in that all data generated in small as well as large scale yielding conditions fall in a scatter band having a constant slope. Finally, the experimental values of J were successfully compared to those calculated by performing elastic-plastic finite element analyses.

## APPENDIX A

The influence of the uncertainty in position of the crack tip on the plastic component of J integral was investigated. After measuring the crack length by using the digital microscope, the position of the crack tip was transferred to the opposite side of the specimen, where the infrared images have been taken. To do that a graph paper with 1 mm grid was fixed on the specimen surface face. A grid line was accurately aligned to the specimen edge by using the digital microscope operating at 20x; therefore, it is estimated that the accuracy in alignment was ( $\pm 0.05$  mm). Due to the geometry resolution of the adopted infrared camera (i.e.  $\pm 23$   $\mu\text{m}$ ), then the overall geometrical accuracy of the crack tip position has been  $\pm 0.075$  mm. Figure 19 reports the ratio between  $J_{\text{max,p}}$  estimated by changing the position of the control volume  $V_c$  by  $\pm 0.075$  mm with respect to the reference value. The analysis has been performed for different applied  $\Delta K_I$  values and it is seen that the maximum variation is in the range  $-11\%/+7\%$ ,

## REFERENCES

- [1] Ellyin F. Fatigue damage, crack growth and life prediction. London: Chapman & Hall, 1997.
- [2] Rice JR, Levy N. Local heating by plastic deformation at a crack tip, in Physics of strength and plasticity, A.S. Argon, ed. M.I.T Press, Cambridge, MA, 1969.
- [3] Loos PJ, Brotzen FR. Localized heat generation during fracture cyclically loaded steel. Metall Mater Trans A 1983; 14A, 1409-19.
- [4] Crupi V, Epasto G, Guglielmino E, Risitano G. Analysis of temperature and fracture surface of AISI4140 steel in very high cycle fatigue regime. Theor Appl Fract Mech 2015; 80, 22-30.
- [5] Kujawsky D, Ellyin F. A fatigue crack propagation model. Eng Fract Mech 1984; 20, 695-04.
- [6] Ranganathan N, Jendoubi K, Benguediab M, Petit J. Effect of R ratio and  $\Delta K$  level on the hysteretic energy dissipated during fatigue crack propagation. Scr Metall 1987; 21 1045-49.



- [7] Kuang JH, Chen YC. Crack initiation load characterization using the critical plastic energy. *Eng Fract Mech* 1996; 53, 571-80.
- [8] Skelton RP, Vilhelmsen T, Webster GA. Energy criteria and cumulative damage during fatigue crack growth. *Int J Fatigue* 1998; 20, 641-49.
- [9] Klingbeil NW. A total dissipated energy theory of fatigue crack growth in ductile solids. *Int J Fatigue* 2003; 25, 117-28.
- [10] Daily JS, Klingbeil NW. Plastic dissipation in fatigue crack growth under mixed-mode loading. *Int J Fatigue* 2004; 26 727-38.
- [11] Mazari M, Bouchouicha B, Zemri M, Banguediab M, Ranganathan N. Fatigue crack propagation analyses based on plastic energy approach. *Comput Mat Sci* 2008; 41 344-49.
- [12] Ranganathan N, Chalon F, Meo S. Some aspects of the energy based approach to fatigue crack propagation. *Int J Fatigue* 2008 ; 30, 1921-29.
- [13] Cojocaru D, Karlsson AM. Assessing plastically dissipated energy as a condition for fatigue crack growth. *Int J Fatigue* 2009 ; 31, 1154-62.
- [14] Daily JS, Klingbeil NW. Plastic dissipation energy at a bimaterial crack tip under cyclic loading. *Int J Fatigue* 2010 ; 32 , 1710-23.
- [15] Nittur PG, Karlsson AM, Carlsson LA. Numerical evaluation of Paris-regime crack growth rate based on plastically dissipated energy. *Eng Fract Mech* 2014; 124-125, 155-66.
- [16] Ondracek J, Materna A. FEM evaluation of the dissipated energy in front of a crack tip under 2D mixed mode loading condition. *Procedia Mater Sci* 2014; 673-78.
- [17] Ranc N, Palin-Luc T, Paris PC. Thermal effect of plastic dissipation at the crack tip on the stress intensity factor under cyclic loading. *Eng Fract Mech* 2011; 78, 61-72.
- [18] Ranc N, Palin-Luc T, Paris PC, Saintier N. About the effect of plastic dissipation in heat at the crack tip on the stress intensity factor under cyclic loading. *Int J Fatigue* 2014 ; 58, 56-65.
- [19] Bhalla KS, Zehnder AT, Han X. Thermomechanics of slow stable crack growth: closing the loop between experiments and computational modelling. *Eng Fract Mech* 2003; 70, 2439-58.
- [20] Jones R, Pitt S. An experimental evaluation of crack energy dissipation. *Int J Fatigue* 2006; 28, 1716-1724
- [21] Fedorova A, Bannikov MV, Plekhov OA. Infrared thermography study of the fatigue crack propagation. *Fracture and Structural Integrity* 2012; 21, 46-53.

- [22] Bär J, Seifert S. Investigation of energy dissipation and plastic zone size during fatigue crack propagation in a high-alloyed steel. *Procedia Mater Sci* 2014; 3, 408-13.
- [23] Maletta C, Bruno L, Corigliano P, Crupi V, Guglielmino E. Crack-tip thermal and mechanical hysteresis in Shape Memory Alloys under fatigue loading. *Mat Sci Eng A-Struct* 2014; 616, 281-87
- [24] Plekhov O, Fedorova A, Kostina A, Pantelev I. Theoretical and experimental study of strain localization and energy dissipation at fatigue crack tip. *Procedia Mater Sci* 2014; 3, 1020-25.
- [25] Breitbarth E, Besel M. Energy based analysis of crack tip plasticity zone of AA2024-T3 under cycling loading, *Int J Fatigue* 2017; 100, 263-273.
- [26] Palumbo D, De Finis R, Demelio GP, Galietti U. Damage monitoring in fracture mechanics by evaluation of the heat dissipated in the cyclic plastic zone ahead of the crack tip with thermal measurements, *Eng Fract Mech* 2017; 181, 65-76.
- [27] Meneghetti G, Ricotta M. Evaluating the heat energy dissipated in a small volume surrounding the tip of a fatigue crack. *Int. J. Fatigue* 2016; 92, 605-615.
- [28] Izyumova A, Plekhov O. Calculation of the energy J-integral in plastic zone ahead of a crack tip by infrared scanning. *Fatigue Fract Eng Mater Struct* 2014; 37, 1330-1337.
- [29] Meneghetti G, Ricotta M. The heat energy dissipated in the material structural volume to correlate the fatigue crack growth rate in stainless steel specimens. *Int J Fatigue* 2018, 115, 107-119.
- [30] Meneghetti G, Ricotta M. The heat energy density averaged in the material structural volume to correlate the fatigue crack growth rate in stainless steel specimens. *Proceedings of 6<sup>th</sup> International Conference on Crack Paths (CP 2018), Verona, Italy, 19-21 September 2018.*
- [31] Rice JR. A path independent integral and the approximate analysis of strain concentration by notches and cracks. *J Appl Mech* 1968; 35, 379-386.
- [32] Pitarresi G, Patterson EA. A review of the general theory of thermoelastic stress analysis. *J Strain Anal Eng Des* 2003;38:405-17.

- [33] Tomlinson RA, Olden EJ. Thermoelasticity for the analysis of crack tip stress fields - a review. *Strain* 1999;35:49-55.
- [34] Stanley P, Chan WK. The determination of stress intensity factors and crack-tip velocities from thermoelastic infra-red emissions. *Proc. Int. Conf. Fatigue Eng. Mater. Struct. (I.Mech.E.)*, Sheffield, UK, 1986, p. 105-14.
- [35] Ju SH, Lesniak JR, Sandor BI. Numerical simulation of stress intensity factors via the thermoelastic technique. *Exp Mech* 1997;37:278-84
- [36] Tomlinson RA, Nurse AD, Patterson EA. Mixed Mode Cracks From Thermoelastic Data. *Fatigue Fract Eng Mater Struct* 1997;20:217-26.
- [37] Dulieu-Barton JM, Fulton MC, Stanley P. Analysis of thermoelastic isopachic data from crack tip stress fields. *Fatigue Fract Eng Mater Struct* 2000;23:301-13.
- [38] Jones R, Krishnapillai M, Cairns K, Matthews N. Application of infrared thermography to study crack growth and fatigue life extension procedures. *Fatigue Fract Eng Mater Struct* 2010;33:871-84
- [39] Bär J, Seifert S. Thermographic Investigation of Fatigue Crack Propagation in a High-Alloyed Steel. *Adv Mater Res* 2014;892:936-41.
- [40] Ancona F, Palumbo D, De Finis R, Demelio GP, Galietti U. Automatic procedure for evaluating the Paris Law of martensitic and austenitic stainless steels by means of thermal methods. *Eng Fract Mech* 2016;163:206-19.
- [41] Urbanek R, Bär J. Influence of motion compensation on lock-In thermographic investigations of fatigue crack propagation. *Eng Fract Mech* 2017;183:13-25.
- [42] Pitarresi G. Lock-In Signal Post-Processing Techniques in Infra-Red Thermography for Materials Structural Evaluation. *Exp Mech* 2015;55:667-80.
- [43] Halford GR. The energy required for fatigue. *J. Mat* 1966; 1(1), 3-18.
- [44] Germain P, Nguyen QS, Suquet P. Continuum Thermodynamics. *Trans. ASME. J Appl Mech* 1983; 50, 1010-1020.

- [45] Lemaitre J, Chaboche JL, Mechanics of solid materials, Cambridge University Press, 1998.
- [46] Chrysochoos A, Louche H. An Infrared image process to analyse the calorific effects accompanying strain localization. *Int J Eng Sci* 2000; 38, 1759-1788.
- [47] Rousselier G. Dissipation in porous metal plasticity and ductile fracture. *J Mechan and Phys Solids* 2001; 49, 1727-1746.
- [48] Chrysochoos A, Berthel B, Latourte F, Galtier A, Pagano S, Watrisse B. Local energy analysis of high cycle fatigue using digital image correlation and infrared thermography. *J Strain Anal* 2008; 43, 411-421.
- [49] Pandey KN, Chand S. Deformation based temperature rise: a review. *Int J Pres Ves Pip* 2003; 80, 673-87.
- [50] Charkaluk E, Constantinescu A. Dissipation and fatigue damage. Proceedings of the Fifth International Conference on Low Cycle Fatigue LCF 5, September 9-11, 2003, Berlin, Germany.
- [51] Plekhov OA, Panteleev IA, Naimark OB. Energy accumulation and dissipation in metals as a result of structural-scaling transitions in a mesodefekt ensemble. *Phys Mesomech* 2007; 10, 294-301.
- [52] G. Meneghetti, M. Ricotta, B. Atzori, A synthesis of the push-pull fatigue behaviour of plain and notched stainless steel specimens by using the specific heat loss, *Fatigue Fract Eng Mater Struct*, 36, 2013, 1306–1322
- [53] Tanaka K, Takahash H, Akiniwa Y. Fatigue crack propagation from a hole in tubular specimens under axial and torsional loading. *Int J Fatigue* 2006; 28, 324-334.
- [54] Dowling, N.E., Mechanical behavior of materials, Pearson Prentice Hall (2007).
- [55] Anderson, T.L., Fracture Mechanics. Fundamentals and Applications, Taylor & Francis Group (2011).

- [56] Wong AK, Sparrow JG, Dunn SA. On the revised theory of the thermoelastic effect. *J Phys Chem Solids* 1988;49:395-400.
- [57] Berto F, Lazzarin P. Relationships between J-integral and the strain energy evaluated in a finite volume surrounding the tip of a sharp and blunt V-notches. *Int J Solids Struct* 2007; 44, 4621-4645.
- [58] Lazzarin P, Zappalorto M. Plastic notch stress intensity factors for pointed V-notches under antiplane shear loading. *Int J Fract* 2008; 152, 1-25.
- [59] Hutchinson JW. Singular behavior at the end of a tensile crack in a hardening material. *J Mech Phys Solids* 1968; 16, 13–31.
- [60] Masing G. Eigenspannungen und Verfestigung beim messing. *Procs of the 2nd Int. Conf. of Applied Mechanics, Zurich, 1926, 332-335.*
- [61] Atzori B, Meneghetti G. Energy dissipation in low cycle fatigue of austempered ductile irons. *Proceedings of the 5th international conference on low cycle fatigue LCF 5, Berlin, Germany, 2003.*
- [62] Meneghetti G, Ricotta M. The use of the specific heat loss to analyse the low- and high-cycle fatigue behaviour of plain and notched specimens made of a stainless steel. *Eng Fract Mech* 2012; 81, 2–17.
- [63] Wan VVC, MacLachlan DW, Dunne FPE. A stored energy criterion for fatigue crack nucleation in polycrystals. *Int J Fatigue* 2014; 68, 90-102.
- [64] Yao Y, Wang J, Keer LM. A phase transformation based method to predict fatigue crack nucleation and propagation in metals and alloys. *Acta Mater* 2017; 127, 241-251
- [65] Brémond P, Potet P. Lock-In Thermography: A tool to analyse and locate thermo-mechanical mechanisms in materials and structures. *Proc. SPIE 4360, Thermosense XXIII, Aerospace/Defense Sensing, Simulation, Control. 2001, Orlando, FL, United States., vol. 4360, 2001, p. 560-6.*

- [66] Meneghetti G, Ricotta M, Atzori B. A two-parameter, heat energy-based approach to analyse the mean stress influence on axial fatigue behaviour of plain steel specimens. *Int J Fatigue* 2016; 82, 60-70.
- [67] Shih CF, Moran B, Nakamura T. Energy release rate along a three-dimensional crack front in a thermally stressed body. *Int J Fract* 1986; 30, 2, 79-102
- [68] Diaz FA, Patterson EA, Tomlinson RA, Yates JR. Measuring stress intensity factors during fatigue crack growth using thermoelasticity. *Fatigue Fract Eng Mater Struct* 2004;27:571-83.
- [69] Marsavina, L., Tomlinson, R. A., Patterson, E.A., Yates, J. R., Investigation of crack closure by using thermoelastic stress analysis, CD-ROM Proc. of the 16th European Conference of Fracture, Alexandroupolis, (2006)

INFRARED THERMOGRAPHY-BASED EVALUATION OF THE ELASTIC-PLASTIC J-INTEGRAL TO CORRELATE  
FATIGUE CRACK GROWTH DATA OF A STAINLESS STEEL

Corresponding author: [giovanni.meneghetti@unipd.it](mailto:giovanni.meneghetti@unipd.it)

HIGHLIGHTS

- An analytical relation temperature field vs elastic-plastic J has been formalised
- Elastic component of J was estimated from thermoelastic stress analysis
- Plastic component of J was estimated from heat dissipation
- The experimental and numerical the elastic-plastic J are in agreement

# INFRARED THERMOGRAPHY-BASED EVALUATION OF THE ELASTIC-PLASTIC J-INTEGRAL TO CORRELATE FATIGUE CRACK GROWTH DATA OF A STAINLESS STEEL

G. Meneghetti<sup>a)</sup>, M. Ricotta<sup>a)</sup>, G. Pitarresi<sup>b)</sup>

<sup>a)</sup> University of Padova, Department of Industrial Engineering, Via Venezia, 1, 35131 Padova – Italy

<sup>b)</sup> University of Palermo, Department of Engineering, Viale delle Scienze, 90128, Palermo - Italy

## CAPTIONS TO FIGURES AND TABLES

Figure 1. (a) Energy balance for a material undergoing fatigue loadings and (b) evolution of the average temperature per cycle.

Figure 2. Propagating fatigue crack and the assumed shape of the control volume  $V_c$  where the heat energy is to be averaged.

Figure 3. Time-variant temperature for  $i$ -th pixel (a) and detailed view (b).

Figure 4. Elastic and plastic components of the strain energy density.

Figure 5. Tested specimen (a), control volume at the crack tip (b) and plastic strain energy density per cycle,  $\bar{W}$ , and plastic component of the strain energy density,  $W_{cc,p}$ , at a point (c).

Figure 6. Specimen geometry ( $r_n=0.1$  mm for  $2\alpha=45^\circ$ ,  $r_n=0.15$  mm for  $2\alpha=90^\circ$ ; thickness is 4 mm; dimensions in mm)



Figure 7. Test setup consisting of a AM4115ZT Dino-lite digital microscope, a FLIR SC7000 infrared camera and a Schenck Hydropuls test machine.

Figure 8 Paris curve of AISI 304L stainless steel.

Figure 9. Crack growth rate vs averaged specific heat energy per cycle

Figure 10. Maps of: (a) Thermoelastic signal  $f$  amplitude; (b) Thermoelastic signal phase; (c) Second Harmonic signal amplitude; (d) Second Harmonic signal phase. The cross sign in all maps provides an estimation of the crack tip position and the circles indicates the points used to calculate  $\Delta K_I$  (sample crack length 10.05 mm, measured  $\Delta K_I=34.4 \text{ MPa}\times\text{m}^{0.5}$ ).

Figure 11. Same as Figure 10 (sample crack length 29.30 mm, measured  $\Delta K_I=67 \text{ MPa}\times\text{m}^{0.5}$ ).

Figure 12. Plots of  $y$  versus  $(1/\Delta T_{\max})^2$ . Face colored points are used in the linear regression to calculate  $\Delta K_I$ .

Figure 13. Cyclic stress-strain curve of the 4-mm-thick hot rolled AISI 304L stainless steel specimens [29].

Figure 14. Plastic strain energy included in the control volume  $V_c$  versus the plastic component of the J integral.

Figure 15. Elastic and plastic components of the J-integral relevant to the experimental tests.

Figure 16. Plastic component of the J-integral versus the size of the control volume for a specimen tested at  $\sigma_g=81 \text{ MPa}$  (a) and  $\sigma_g=120 \text{ MPa}$  (b) ( $J_{\max,p}$  evaluated according to Eq. (25)).

Figure 17. Crack propagation rates versus the J-integral range evaluated from temperature measurements.

Figure 18. Comparison between FE results and the scatter band fitted on the experimental values of  $\Delta J$  in Figure 17.

Figure 19. Sensitivity of  $J_{\max,p}$  estimations on the uncertainty of the crack tip position (see Figure 2).

Table 1: Mechanical properties and chemical composition of the AISI 304L stainless steel [29].

ACCEPTED MANUSCRIPT

## FIGURES

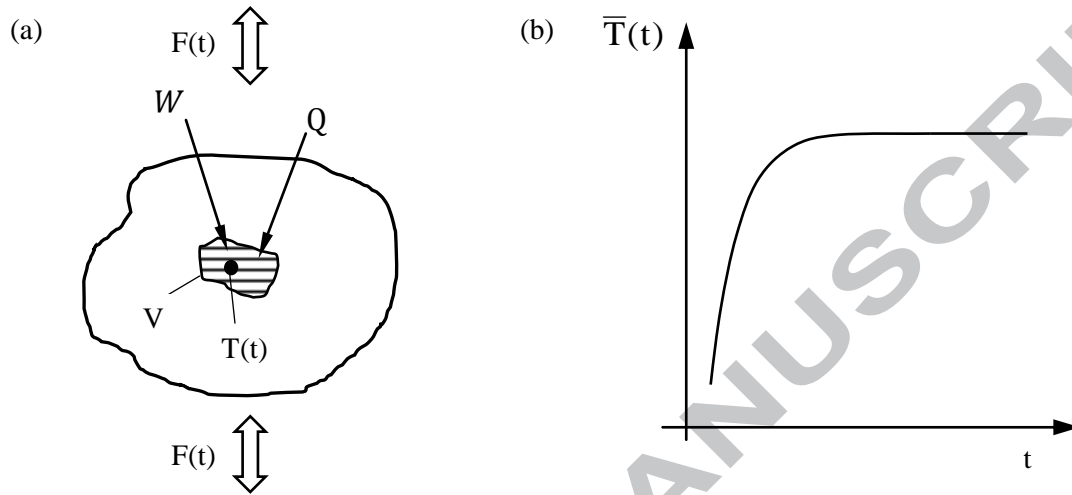


Figure 1. (a) Energy balance for a material undergoing fatigue loadings and (b) evolution of the average temperature per cycle.

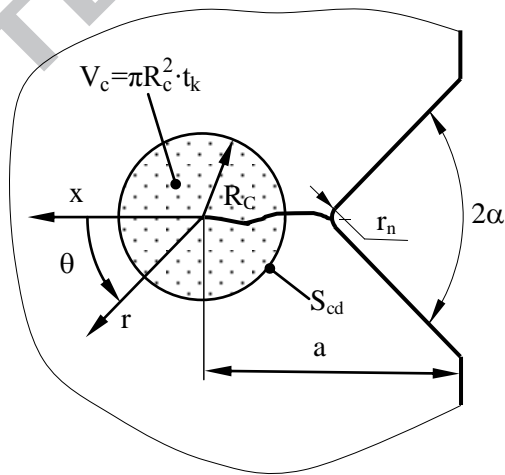


Figure 2. Propagating fatigue crack and the assumed shape of the control volume  $V_c$  where the heat energy is to be averaged.

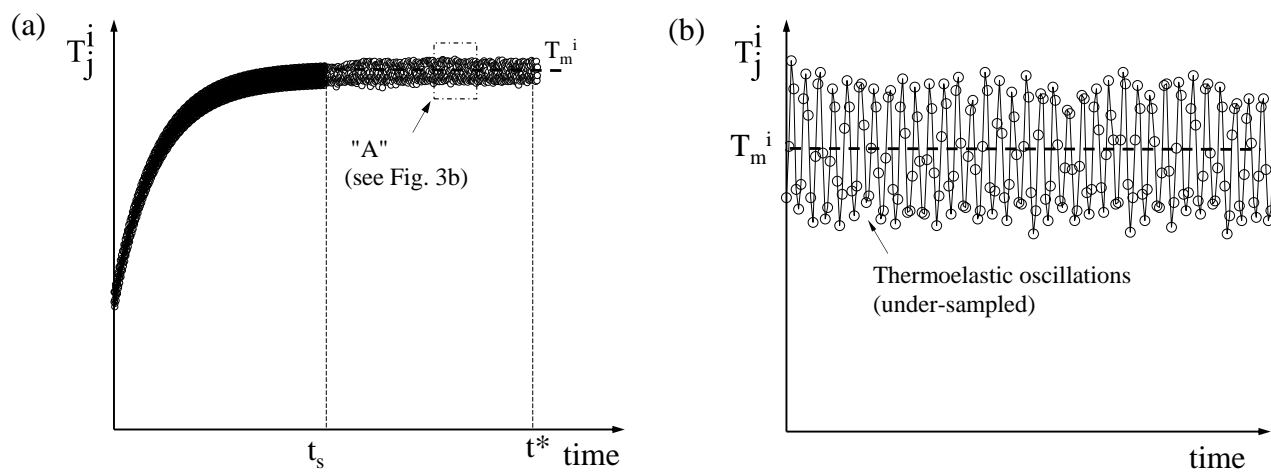


Figure 3. Time-variant temperature for  $i$ -th pixel (a) and detailed view (b).

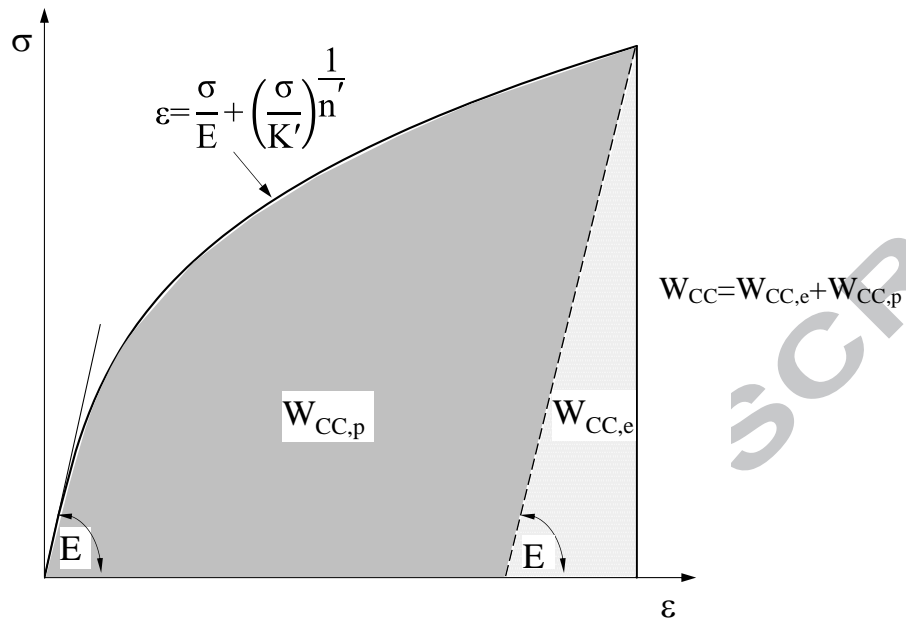


Figure 4. Elastic and plastic components of the strain energy density.

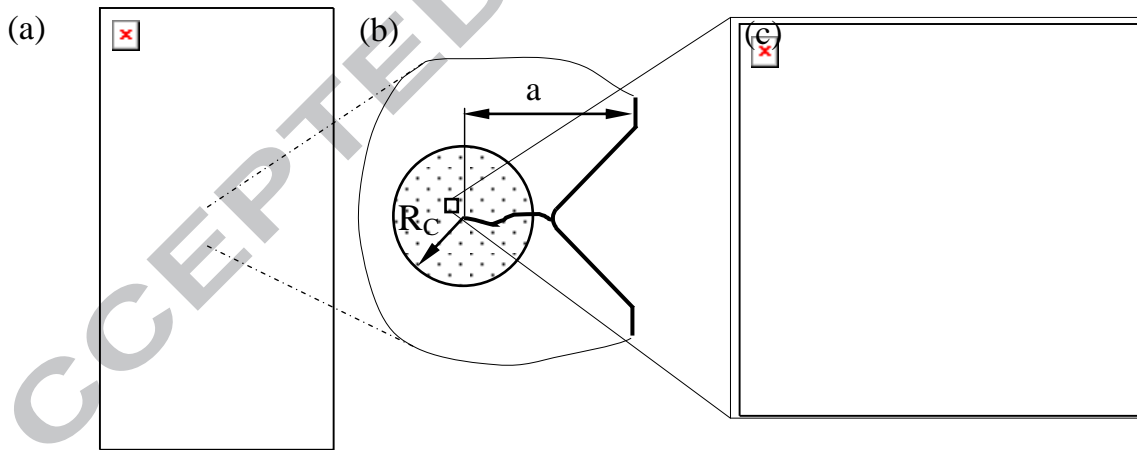


Figure 5. Tested specimen (a), control volume at the crack tip (b) and plastic strain energy density per cycle,  $\bar{W}$ , and plastic component of the strain energy density,  $W_{cc,p}$ , at a point (c).

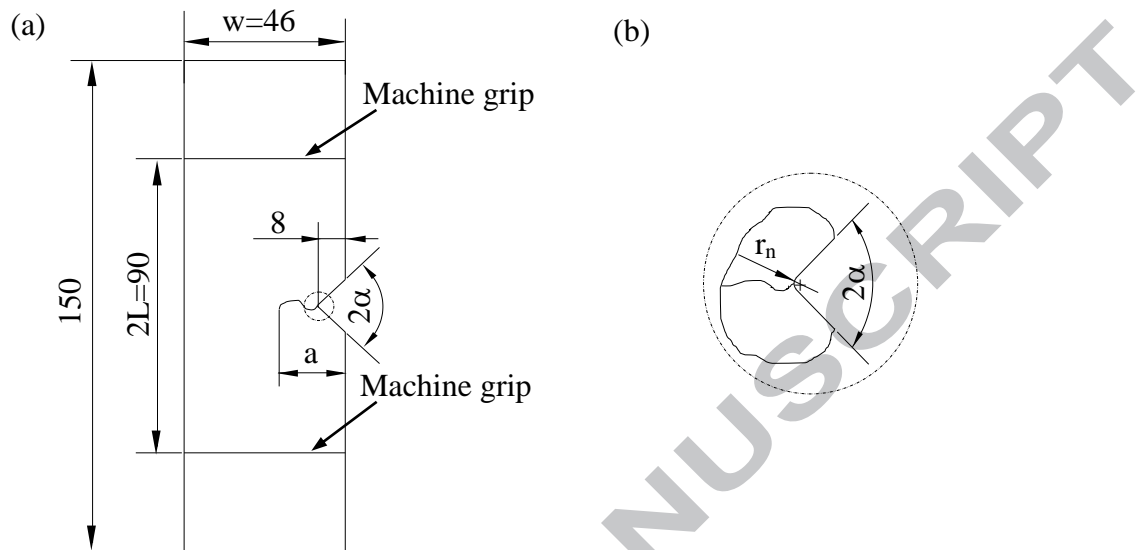


Figure 6. Specimen geometry ( $r_n=0.1$  mm for  $2\alpha=45^\circ$ ,  $r_n=0.15$  mm for  $2\alpha=90^\circ$ ; thickness is 4 mm; dimensions in mm)

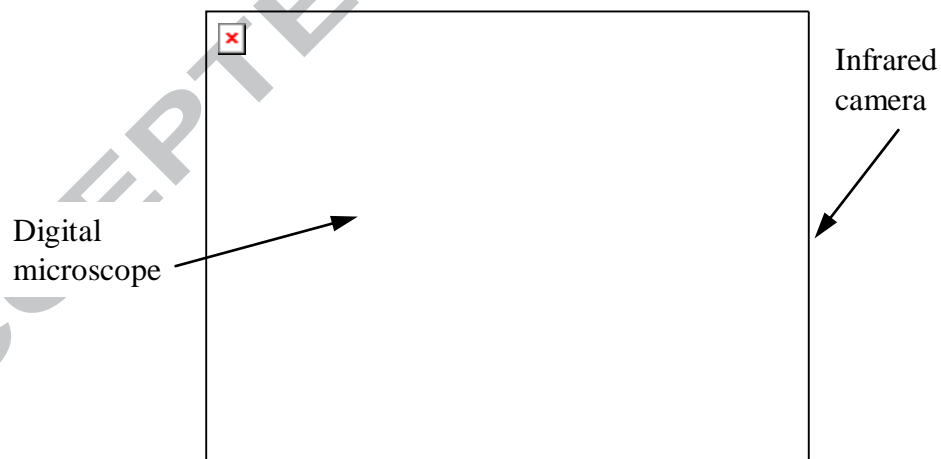


Figure 7. Test setup consisting of a AM4115ZT Dino-lite digital microscope, a FLIR SC7000 infrared camera and a Schenck Hydropuls test machine.

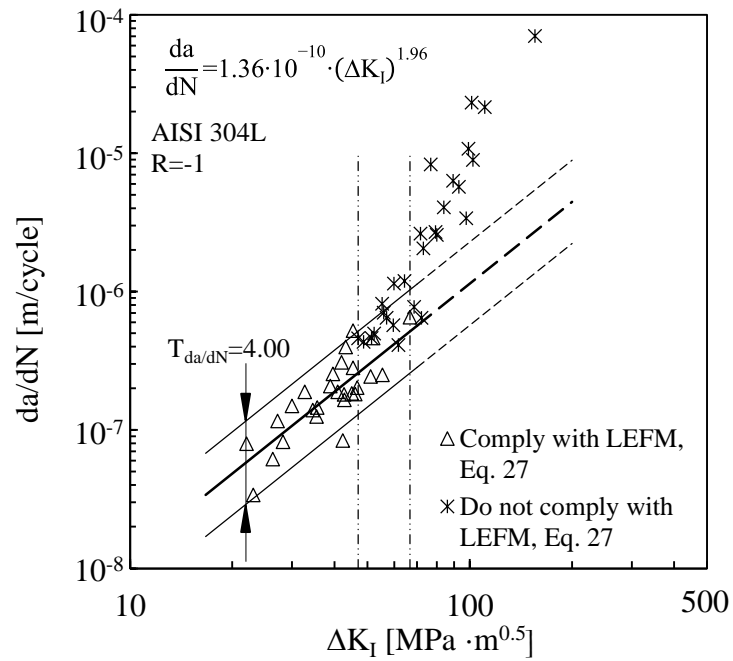


Figure 8. Paris curve of AISI 304L stainless steel.

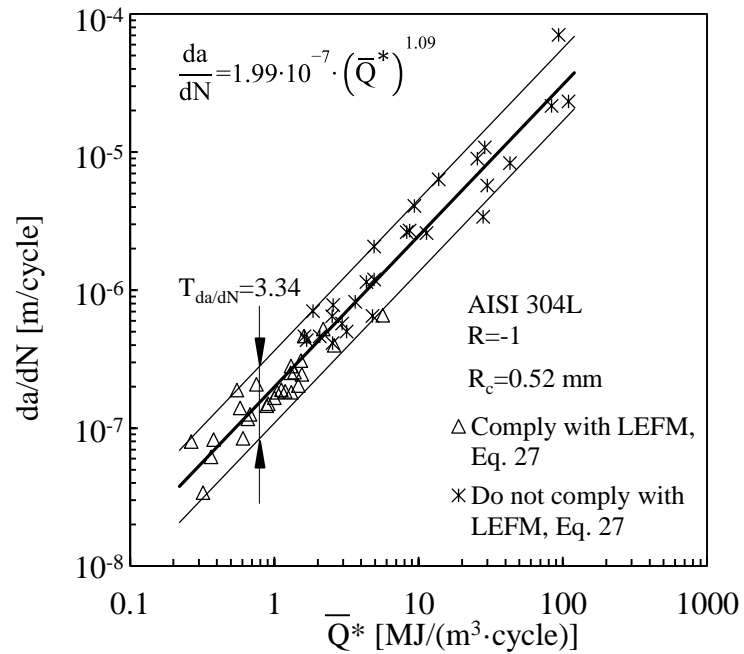


Figure 9. Crack growth rate vs averaged specific heat energy per cycle

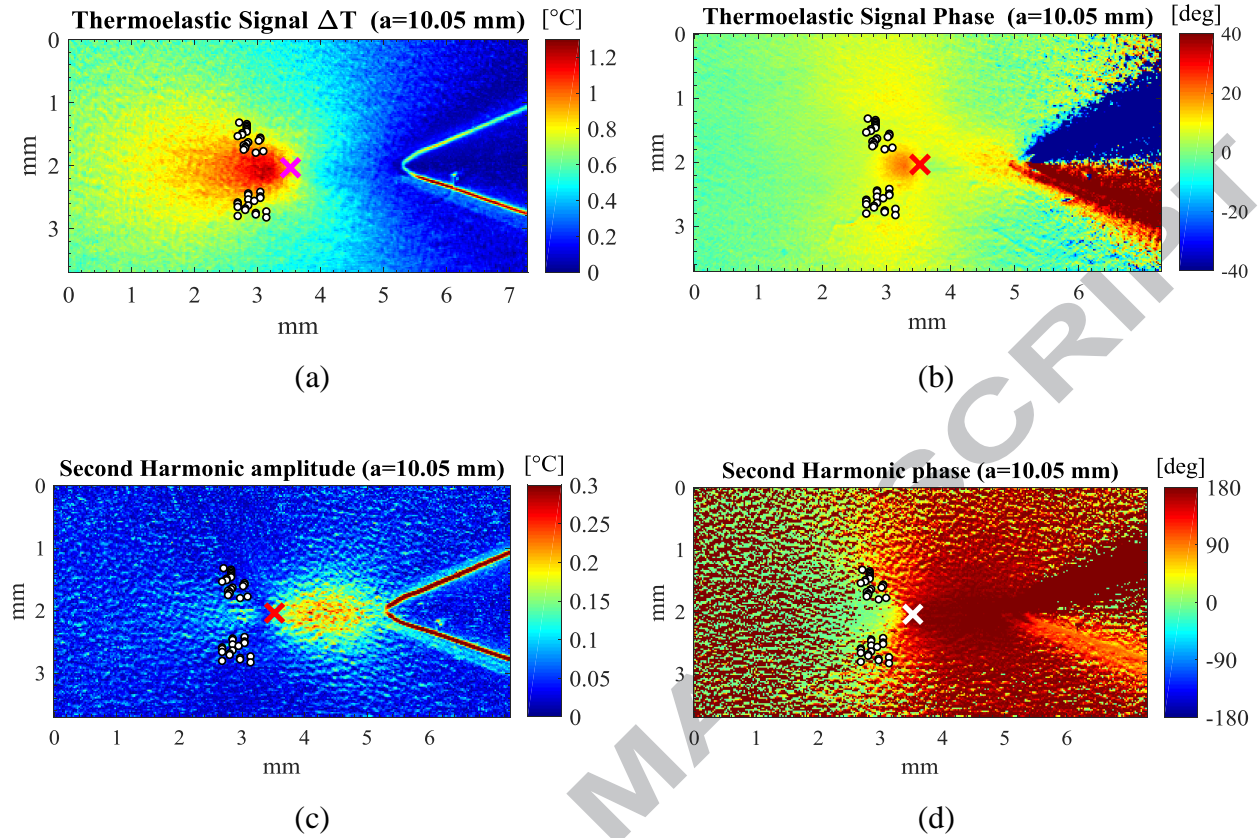


Figure 10. Maps of: (a) Thermoelastic signal  $f$  amplitude; (b) Thermoelastic signal phase; (c) Second Harmonic signal amplitude; (d) Second Harmonic signal phase. The cross sign in all maps provides an estimation of the crack tip position and the circles indicates the points used to calculate  $\Delta K_I$  (sample crack length 10.05 mm, measured  $\Delta K_I=34.4 \text{ MPa}\times\text{m}^{0.5}$ ).



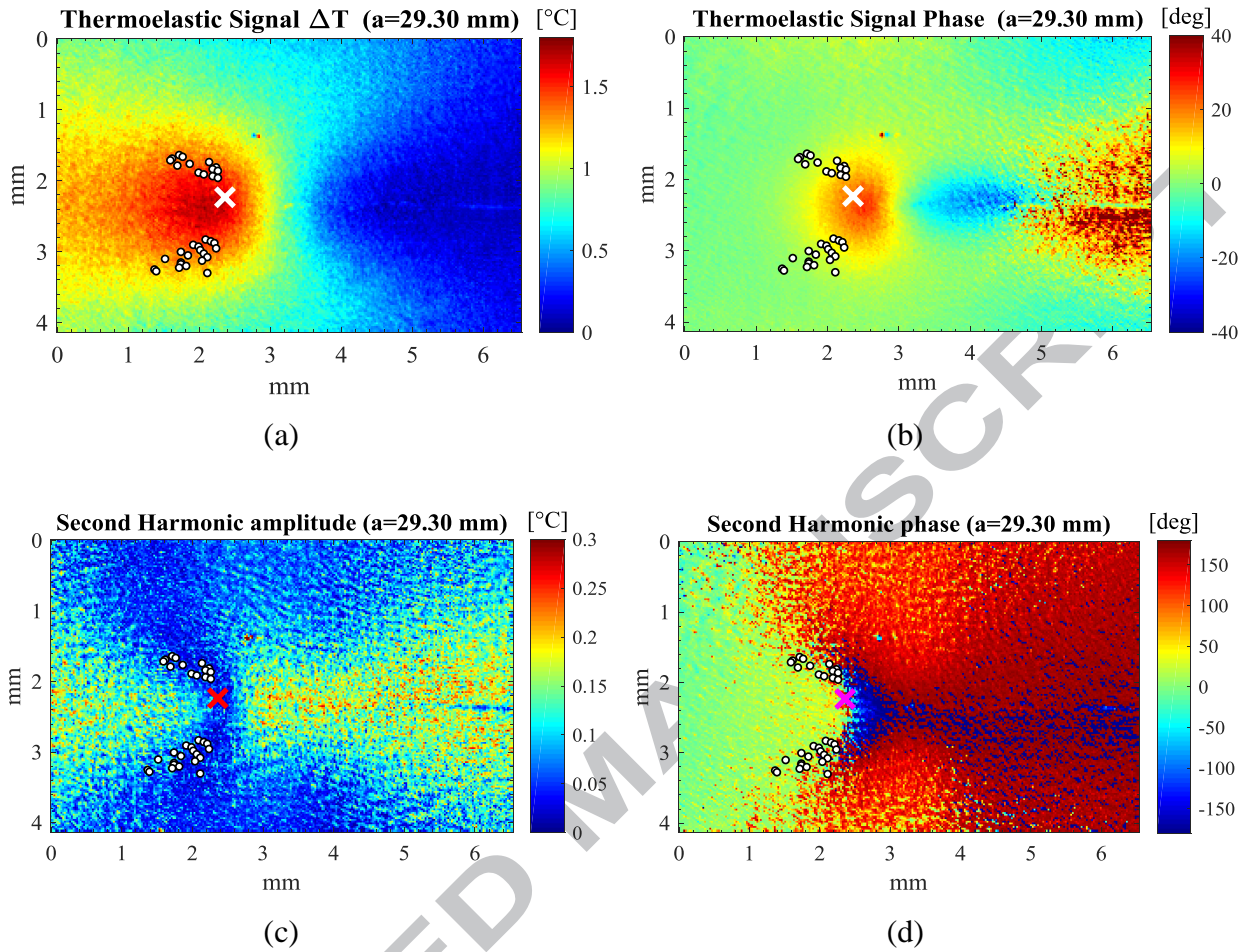


Figure 11. Same as Figure 10 (sample crack length 29.30 mm, measured  $\Delta K_I=67 \text{ MPa}\times\text{m}^{0.5}$ ).

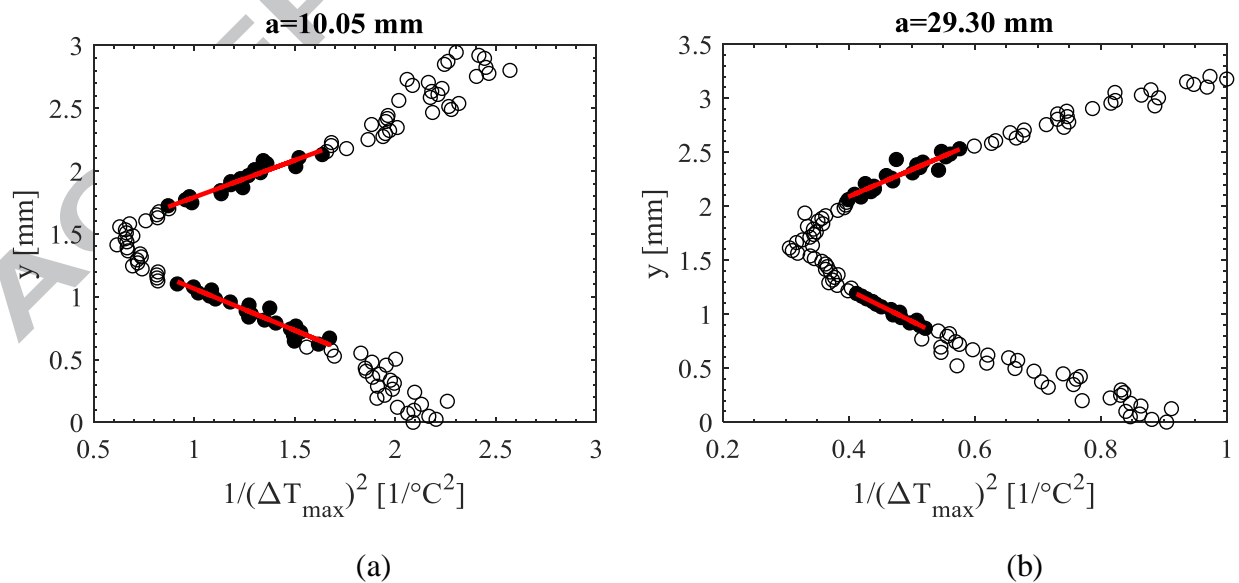


Figure 12. Plots of  $y$  versus  $(1/\Delta T_{\max})^2$ : (a) test with crack length  $a=10.05$  mm; (b) test with crack length  $a=29.30$  mm. Face colored points are used in the linear regression to calculate  $\Delta K_I$ .

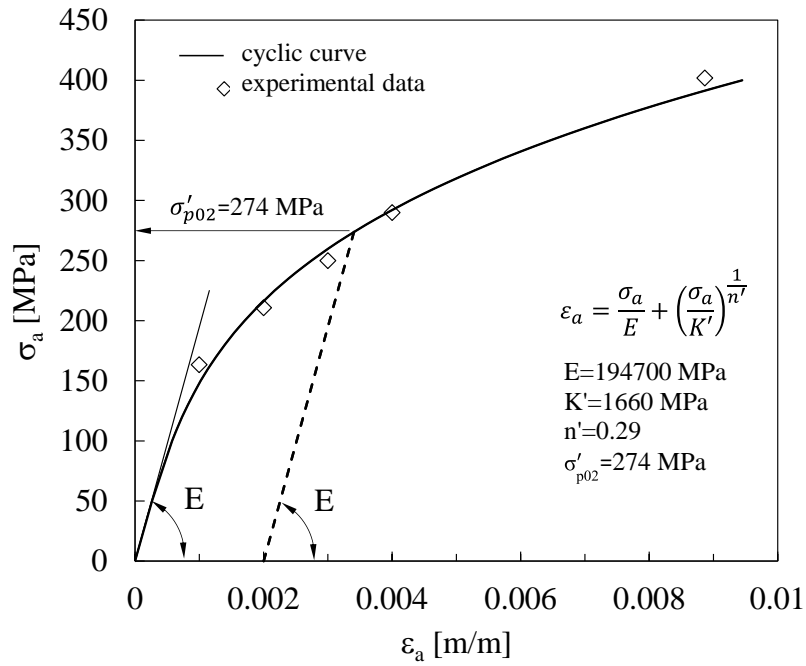


Figure 13. Cyclic stress-strain curve of the 4-mm-thick hot rolled AISI 304L stainless steel specimens [29].

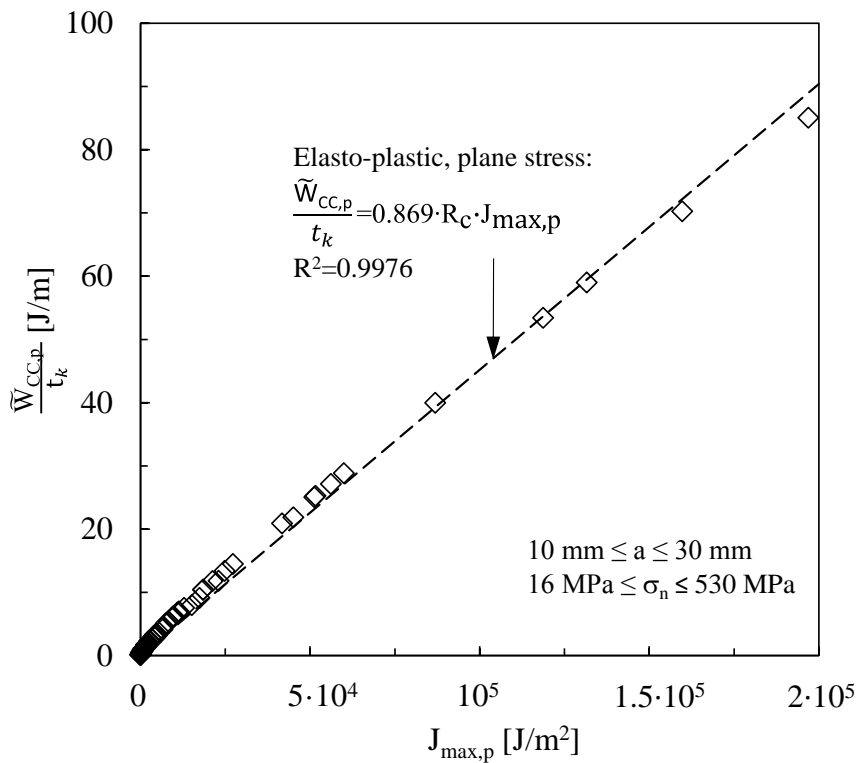


Figure 14. Plastic strain energy included in the control volume  $V_c$  versus the plastic component of the J integral.

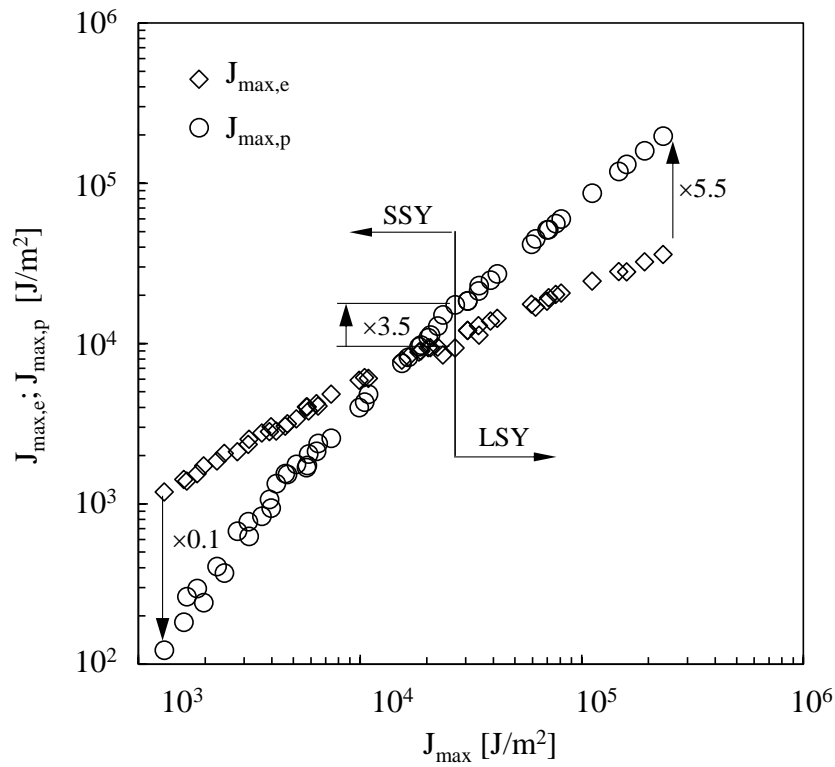
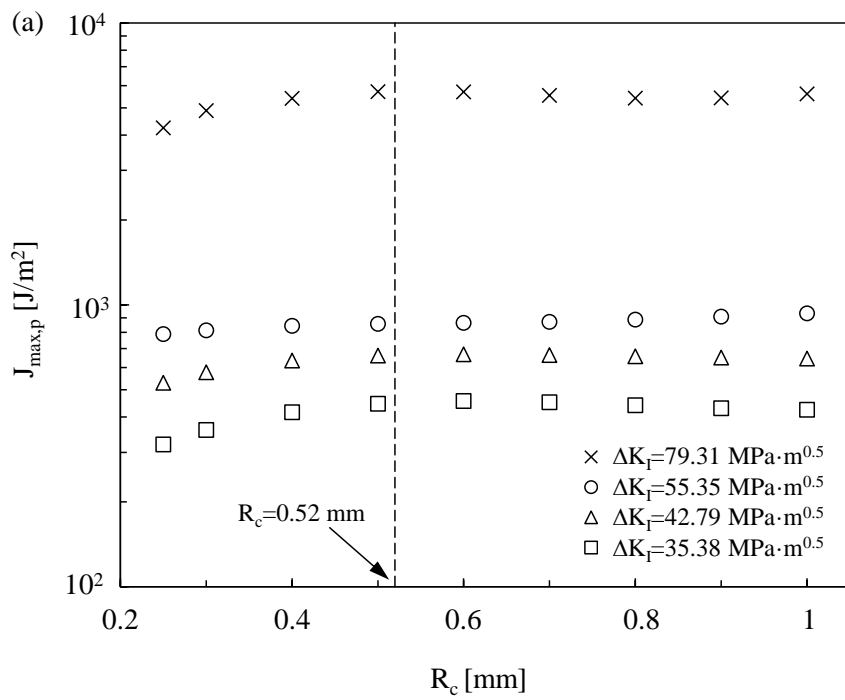


Figure 15. Elastic and plastic components of the J-integral relevant to the experimental tests.



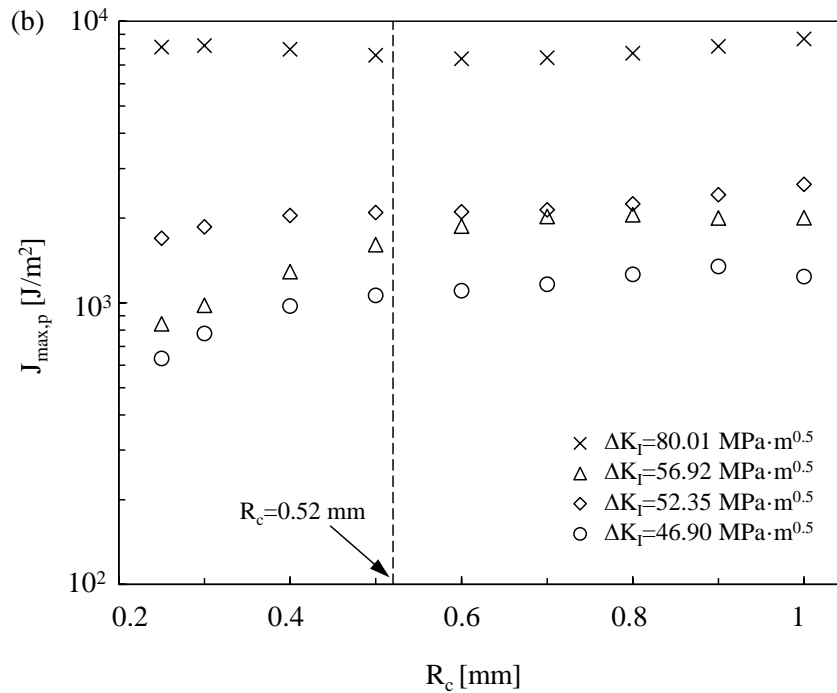


Figure 16. Plastic component of the J-integral versus the size of the control volume for a specimen tested at  $\sigma_g=81$  MPa (a) and  $\sigma_g=120$  MPa (b) ( $J_{\max,p}$  evaluated according to Eq. (25)).

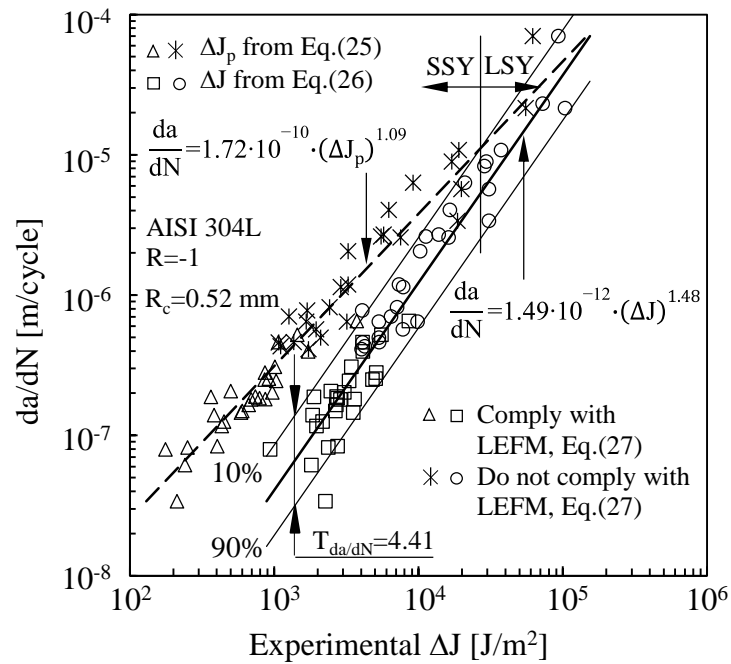


Figure 17. Crack propagation rates versus the J-integral range evaluated from temperature measurements.

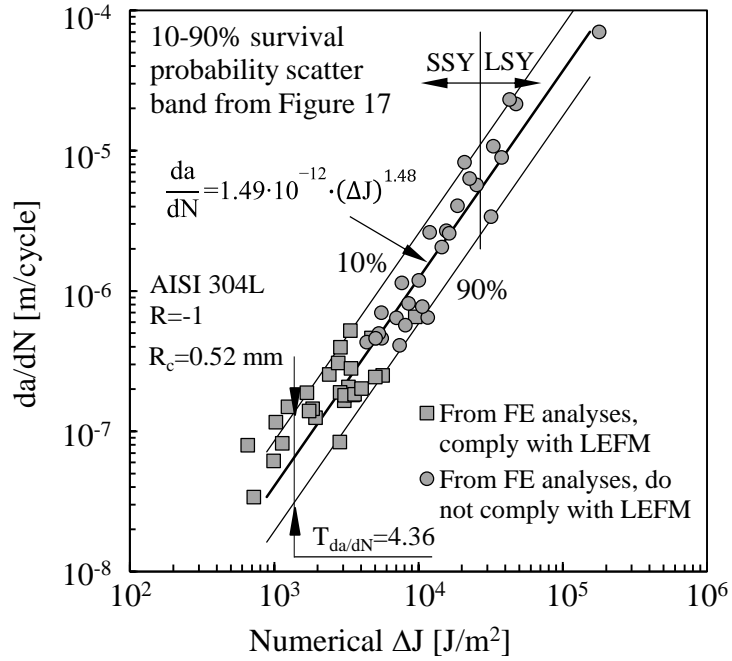


Figure 18. Comparison between FE results and the scatter band fitted on the experimental values of  $\Delta J$  in Figure 17.

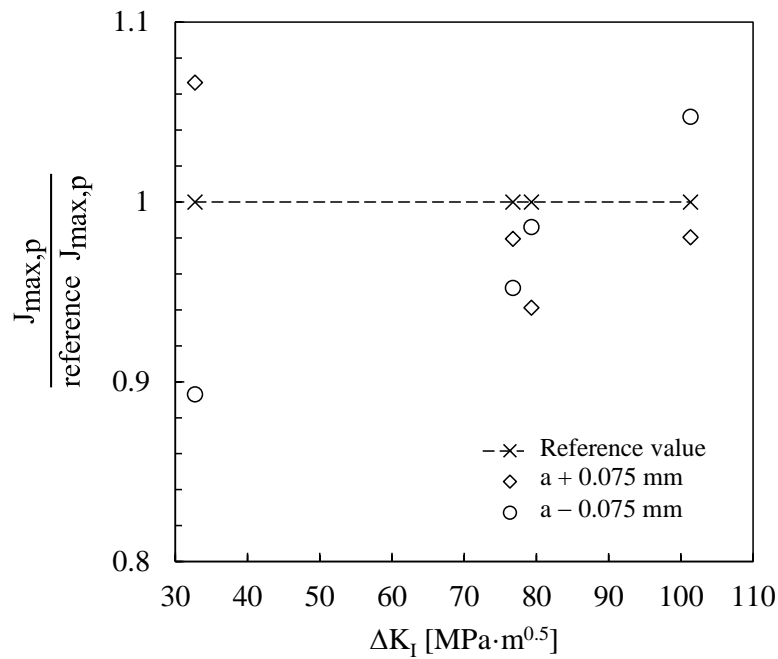


Figure 19. Sensitivity of  $J_{max,p}$  estimations on the uncertainty of the crack tip position (see Figure 2).

## TABLES

Table 1: Mechanical properties and chemical composition of the AISI 304L stainless steel [29].

$\sigma_{p0.2}$	$\sigma_R$	A	$\sigma_{A-1}$	HB	C	Mn	Si	Cr	Ni	P	S	N
[MPa]	[MPa]	[%]	[MPa]		[w%]	[w%]	[w%]	[w%]	[w%]	[w%]	[w%]	[w%]
279	620	57	202	170	0.026	1.470	0.370	18.100	8.200	0.034	0.001	0.058